A&A 392, 585–598 (2002)
DOI: 10.1051/0004-6361:20021188

Astronomy & Astrophysics

Simultaneous X-ray spectroscopy of YY Gem with *Chandra* and *XMM-Newton*

B. Stelzer[1], V. Burwitz[1], M. Audard[2], M. Güdel[2], J.-U. Ness[3], N. Grosso[1], R. Neuhäuser[1], J. H. M. M. Schmitt[3], P. Predehl[1], and B. Aschenbach[1]

[1] Max-Planck-Institut für extraterrestrische Physik, Postfach 1312, 85741 Garching, Germany
[2] Paul Scherrer Institut, Würenlingen & Villigen, 5232 Villigen PSI, Switzerland
[3] Hamburger Sternwarte, Gojenbergsweg 112, 21029 Hamburg, Germany

Received 25 March 2002 / Accepted 20 June 2002

Abstract. We report on a detailed study of the X-ray spectrum of the nearby eclipsing spectroscopic binary YY Gem. Observations were obtained simultaneously with both large X-ray observatories, *XMM-Newton* and *Chandra*. We compare the high-resolution spectra acquired with the Reflection Grating Spectrometer onboard *XMM-Newton* and with the Low Energy Transmission Grating Spectrometer onboard *Chandra*, and evidence in direct comparison the good performance of both instruments in terms of wavelength and flux calibration. The strongest lines in the X-ray spectrum of YY Gem are from oxygen. Oxygen line ratios indicate the presence of a low-temperature component (1–4 MK) with density $n_e \leq 2\times10^{10}$ cm^{-3}. The X-ray lightcurve reveals two flares and a dip corresponding to the secondary eclipse. An increase of the density during phases of high activity is suggested from time-resolved spectroscopy. Time-resolved global fitting of the European Photon Imaging Camera CCD spectrum traces the evolution of temperature and emission measure during the flares. These medium-resolution spectra show that temperatures $>10^7$ K are relevant in the corona of YY Gem although not as dominant as the lower temperatures represented by the strongest lines in the high-resolution spectrum. Magnetic loops with length on the order of 10^9 cm, i.e., about 5% of the radius of each star, are inferred from a comparison with a one-dimensional hydrodynamic model. This suggests that the flares did not erupt in the (presumably more extended) inter-binary magnetosphere but are related to one of the components of the binary.

Key words. X-rays: stars – stars: individual: YY Gem – stars: late-type, coronae, activity

1. Introduction

The Castor system comprises three visual stars, all of which are spectroscopic binaries. The optically faintest of the three components, YY Gem (=Castor C), is of major importance to stellar evolution studies: being an eclipsing spectroscopic binary ($i \sim 86°$; Pettersen 1976) very near or on the main sequence it allows for the determination of masses and radii of both components, and for a test of evolutionary tracks. Both stars in the YY Gem system are of nearly equal spectral type, dM1e, in a synchronous orbit with a period of 0.81 d. YY Gem was the first late-type star on which periodic photometric variability was detected (Kron 1952). Bopp & Evans (1973) have explained similar brightness variations on the flare star BY Dra by rotation of star spots, and stars displaying this phenomenon are since then termed BY Dra variables. Doppler images of YY Gem have revealed spots at mid-latitudes on both stars (Hatzes 1995).

X-rays from the Castor sextuplet were first recorded by the *Einstein* satellite (Vaiana et al. 1981; Caillault 1982; Golub et al. 1983). Since then the system was observed by virtually all X-ray observatories; see e.g., Pallavicini et al. (1990), Gotthelf et al. (1994), Schmitt et al. (1994), Güdel et al. (2001a). As the spatial resolution of the instruments improved, X-ray emission from individual members of the Castor system could be identified. At present, all three visual binaries in the sextuplet are known to be X-ray sources. The X-ray emission from Castor A and B is commonly attributed to their late-type companions because the primaries, being early A-type stars without a convective envelope and consequently with no ability to support the dynamo mechanism, are not expected to be X-ray sources.

In nearly all of the previous X-ray studies of YY Gem flare activity was reported. The luminosity of YY Gem in the soft X-ray band ranges between $\sim(2–8)\times10^{29}$ erg/s. Flares have been observed also in other parts of its electromagnetic spectrum. Doyle & Mathioudakis (1990) found that the flare activity on YY Gem is more than an order of magnitude larger during out-of-eclipse times as compared to times when one of the stars is eclipsed. On the basis of these *U* band observations it was suggested that the amount of magnetic energy is largest in the inter-binary space, leading to frequent energy release in this region. A periodicity of the optical flaring rate was reported by Doyle et al. (1990), but has not been confirmed so far.

Send offprint requests to: B. Stelzer,
e-mail: stelzer@xray.mpe.mpg.de

The chromosphere and transition region was examined by Haisch et al. (1990), and moderate variability throughout the orbital cycle was detected in the emission lines.

The extraordinary variability of YY Gem has instigated us to carry out a coordinated multi-wavelength campaign comprising radio, optical and X-ray observations. As a unique example of an eclipsing spectroscopic binary with nearly identical components YY Gem is ideally suited for a study of stellar coronal structure. In particular we were aiming at looking into the possibility of enhanced flare activity in the inter-binary space as suggested by Doyle & Mathioudakis (1990). Magnetic structures in between the components of binaries have been discussed also for RS CVn systems (e.g., Uchida & Sakurai 1983). Additional information about the coronal geometry can be obtained from observations of X-ray eclipses. The depth and duration of the eclipses provide a measure for the spatial extent of the corona and contribution of the two components in the binary. From a 3D-deconvolution of the X-ray lightcurve of YY Gem (using an earlier observation by *XMM-Newton*) Güdel et al. (2001a) found that the coronae of both stars in the binary are inhomogeneously structured with brighter areas at mid-latitudes. Obscuration of coronal features can also be used to localize and constrain the emitting region in active stars (see e.g., Gunn et al. 1997, 1999; Schmitt & Favata 1999).

As part of our multi-wavelength project the Castor system was observed simultaneously with both *XMM-Newton* and *Chandra*. While in the EPIC MOS image presented by Güdel et al. (2001a) Castor A and B were spatially resolved, our *Chandra* observation allows for the first time to separate the X-ray spectra of Castor A and B from each other. We will examine the X-ray characteristics of Castor A and B in a related publication (Stelzer et al., in prep.). Here we concentrate on the intermediate and high-resolution X-ray spectrum of YY Gem. We emphasize that this observation presents an excellent opportunity to cross-check the calibration of the dispersive instruments onboard both satellites. We analyse the emission line spectrum observed with the *Chandra* Low-Energy Transmission Grating Spectrometer (LETGS) and the Reflection Grating Spectrometer (RGS) onboard *XMM-Newton* independently of each other, and derive observed line fluxes for both instruments. Emission lines in the spectral region of the LETGS and RGS include the helium-like triplets from C V to Si XIII, the Lyman series of hydrogen-like ions, and numerous iron L-shell transitions. By means of time-resolved analysis of spectral parameters we check for spectral variability related to changes in the activity level of YY Gem. We use both "global" fits to the EPIC X-ray spectrum from 0.3 to 10 keV and modeling of individual emission lines in the range 2–175 Å (resolved by the gratings onboard both *Chandra* and *XMM-Newton*) to infer the time evolution of temperature and density of the emitting plasma.

The *XMM-Newton* and *Chandra* observations are introduced in Sect. 2. In Sect. 3 we present results from high-resolution spectroscopy, involving a detailed comparison of the contemporaneous LETGS and RGS spectrum. Time-resolved spectroscopy is discussed in Sect. 4. We draw conclusions on the coronal structure by means of loop modeling (Sect. 5), and summarize the results in Sect. 6.

2. Observations

YY Gem was observed by both *Chandra* (Obs-ID 28) and *XMM-Newton* (Obs-ID 0112880801) on Sep. 29/30 2000 for a total observing time of 59 ksec and 55 ksec, respectively. Both observations were part of the Guaranteed Time program. X-ray lightcurves obtained with the individual instruments demonstrating the times of observation are shown in Fig. 1.

We have computed the orbital phases for the time of observation using the ephemeris of Torres & Ribas (2002). Two large flare events, the secondary eclipse, a flare-like feature after secondary eclipse, and an extended "high state" at the end of the *Chandra* observation are seen. The structure of the X-ray lightcurve resembles that of the earlier *XMM-Newton* observation of YY Gem made in April 2000 (Güdel et al. 2001a). The larger of the two flares and the feature after secondary eclipse are seen at similar orbital phases in both observations.

2.1. XMM-Newton

The *XMM-Newton* observation on Sep. 29/30, 2000 was carried out in full-frame mode of both EPIC instruments and with the thick filter inserted for both pn and MOS to avoid optical loading from Castor. The Optical Monitor was in closed position due to the optical brightness of the Castor system. For a description of the X-ray instruments onboard *XMM-Newton* see Jansen et al. (2001), den Herder et al. (2001), Strüder et al. (2001), Turner et al. (2001), and Aschenbach (2002).

For the analysis of the EPIC spectrum source photons were selected from a circular region centered on the position of YY Gem. An appropriate outer radius for the extraction of source photons is the value where the background subtracted radial distribution of integrated counts flattens out, in this case ∼26″. With this choice we make sure that the data are not contaminated by contributions from Castor AB (at a separation of 74″ from YY Gem). A background spectrum was extracted from a nearby position with the same area as the source extraction region. The EPIC data were analysed with the *XMM-Newton* Science Analysis Software (SAS) version from May 2000. We used the pn detector response made available by the hardware team in April 2001 and the MOS responses released in February 2001 (see Sect. 4.2.1 for more details). The RGS data were analysed with the SAS version 5.2. CCD PI filtering allows to separate the orders. We concentrate on the first order spectrum. The background spectrum is obtained from a region offset from the spectrum of YY Gem and Castor AB in the cross-dispersion direction.

2.2. Chandra

With *Chandra* we used the LETGS combining the Low-Energy Transmission Grating (LETG) with the High Resolution Camera (HRC) (see Brinkman et al. 2000). The *Chandra* observation began ∼2.5 h after the start of the pointing with *XMM-Newton*. After the *XMM-Newton* observation ended *Chandra* continued to observe for ∼5 h (see Fig. 1).

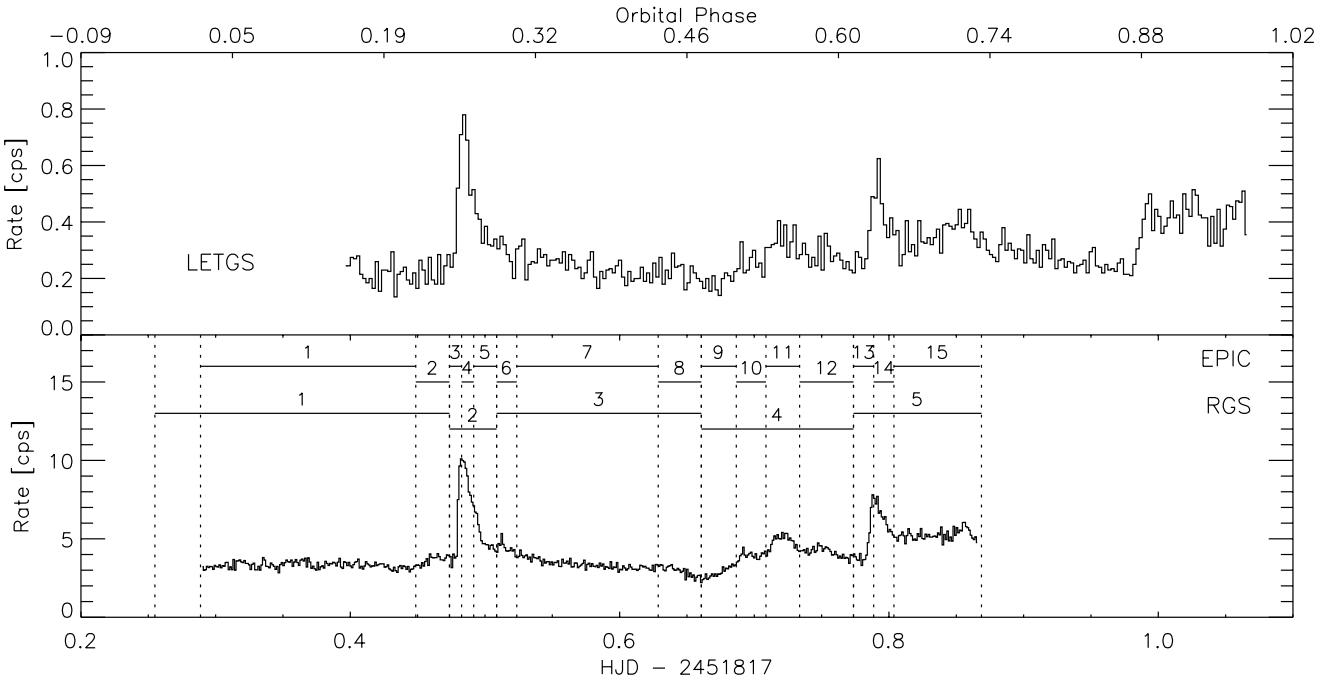

Fig. 1. Background subtracted X-ray lightcurve of YY Gem on 2000 Sep. 29/30. *Top* – *Chandra* LETG zeroth order with 200 s binsize, *bottom* – *XMM-Newton* EPIC pn with 100 s binsize. The orbital phase was computed with the ephemeris by Torres & Ribas (2002). The time intervals selected for time-resolved spectroscopy are indicated by horizontal lines above the lightcurves.

The data obtained from the *Chandra* science center was reprocessed following the CIAO 2.1 science threads[1] for applying the newest degap-corrections to the HRC-S data as well as generating new event level 2 files, in which background is reduced significantly by a spatially dependent "light pha filtering" described in the thread.

The spectra were then extracted from these event files using IDL routines. For the source we used the "bow tie" extraction region as described in the *Chandra* Proposers' Observatory Guide[2] (POG). Large areas above and below the source extraction region were selected for the background, such that the ratio between source and background area is 7.5 (see Fig. 1 in Burwitz et al. 2001 for an illustration). Towards longer wavelengths $\lambda > 48.4$ Å the background regions become wider in order to maintain the constant ratio of areas between source and background spectral bins.

3. High-resolution spectroscopy

In this section we present and compare results from the high-resolution dispersive instruments on *Chandra* and *XMM-Newton*. We took care that the Castor AB components are excluded from the background extraction regions. Lists of all identified lines are given in Tables 1 and 2. We derive photon fluxes and use line ratios for coronal plasma diagnostics. In this context the triplets of He-like ions comprising the resonance line r, the intercombination line i, and the forbidden line f, are of particular interest as their intensity ratios $R = f/i$ and $G = (f+i)/r$ provide an estimate for the electron density n_e and electron temperature T_e of the respective lines. The temperature sensitivity of G is due to the collisional excitation rates which have different temperature dependence for the resonance line compared to the forbidden and intercombination line. The G ratio also indicates whether the plasma is dominated by collisions or photo-ionization: a strong r line corresponds to collisionally dominated plasmas ($G \sim 1$), while r is weak in photo-ionized environments with $G > 4$ (see Porquet & Dubau 2000). We caution that a given line does actually form over an extended range of temperatures in a non-isothermal plasma, and thus the temperature derived from G may be misleading. The number of collisions increases with density. As a consequence the upper level of the f transition is depopulated and fills the upper level of the i transition. This results in a decrease of R with increasing n_e. Only in the low- and high-density limits is R independent of n_e.

3.1. Line identifications

We extracted and analysed the RGS and the LETGS spectra of YY Gem as described in Sects. 2.1 and 2.2. The time-averaged LETGS spectrum in the wavelength range from 0−100 Å is displayed in Fig. 2. We have added left (negative) and right (positive) side of the spectrum. Above 100 Å only few lines are seen, all from highly ionized iron. A close-up of the region with the strongest emission lines is shown in Fig. 3 together with the time-averaged first order RGS spectrum in the same wavelength region. We show the spectrum in units of cts/s/bin. Since the RGS and the LETGS observations overlap for about 75% in time, the measured line fluxes should be similar. The count rates are higher for RGS than for LETGS throughout

[1] http://asc.harvard.edu/ciao/documents-threads.html
[2] http://asc.harvard.edu/udocs/docs/docs.html

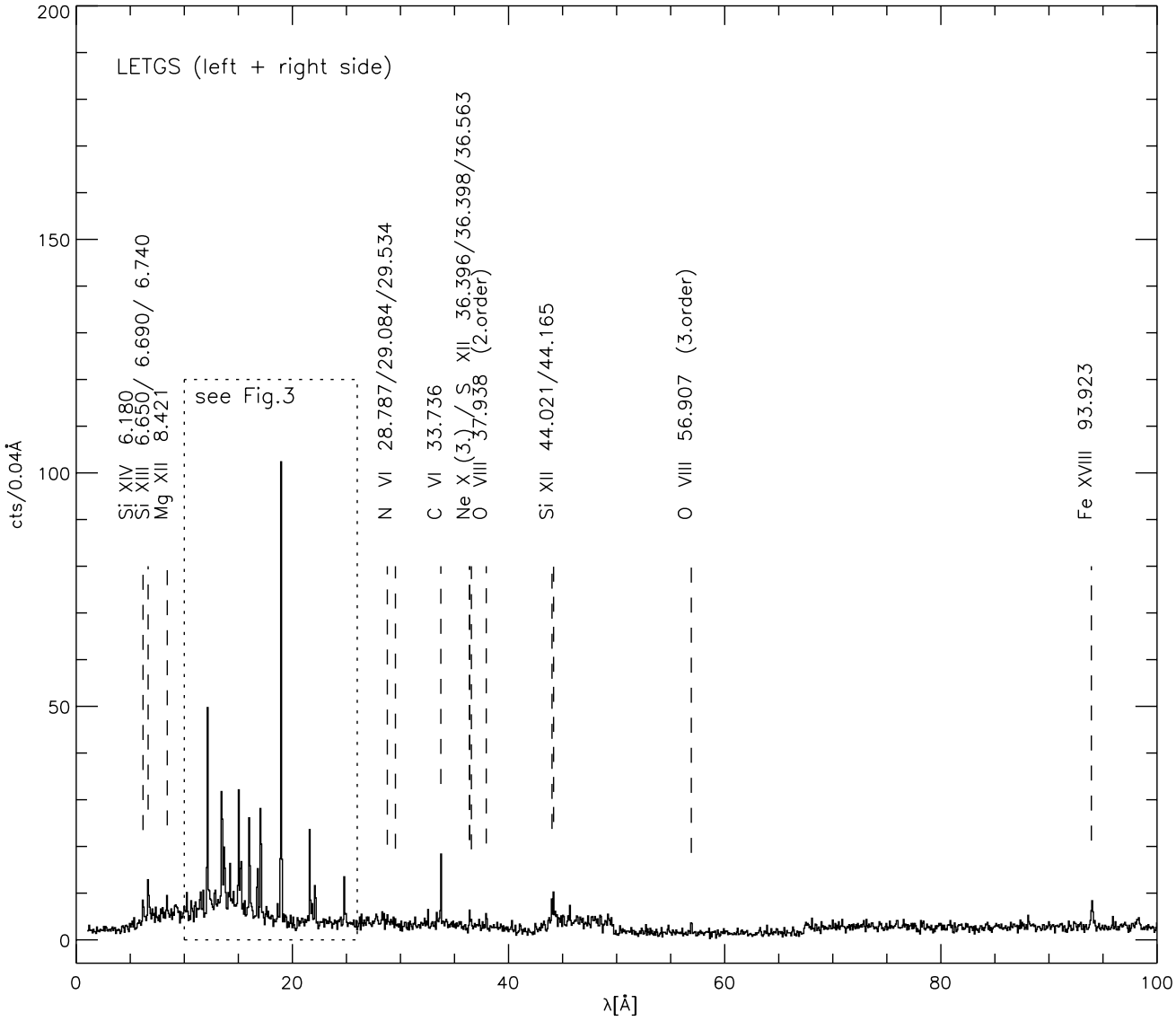

Fig. 2. Time-averaged *Chandra* LETGS spectrum (left and right side added); total exposure time is 58 ksec, and binsize is 0.04 Å. Only few emission lines are identified above 100 Å (108.4 Å, 117.2 Å, 128.73 Å, and 132.9 Å; not displayed here). The region within the dotted rectangle (10−26 Å) is shown in more detail in Fig. 3.

most of the displayed spectral region, and demonstrate directly the higher sensitivity of the RGS, except at wavelengths ≤10 Å. The full wavelength range of the RGS extends from 6−35 Å. However, the only lines found in the RGS spectrum of YY Gem outside the range displayed in Fig. 3 are the silicon lines between 6−7 Å, the resonance line of the triplet of He-like N VI, and transitions from H-like carbon.

We identified the most prominent lines in both the LETGS and the RGS spectrum. The line centers and fluxes were determined with the CORA[3] line fitting application (Ness et al. 2001). CORA was designed for low count rate spectra, based on Poisson statistics and employs a maximum likelihood method to determine the best fit parameters. The background is treated as a constant in the vicinity of individual lines. For the LETGS spectrum we used Gaussians to approximate the line profile. To avoid artificial broadening of lines resulting from uncertainties in the wavelength calibration, the positive and negative sides of the spectrum were analysed separately. Then we checked the agreement, and if adequate, we merged the positive and negative sides to increase the signal for the analysis of line ratios. For RGS Lorentzians represent a better approximation to the instrumental profile. To improve the S/N the first order spectra of RGS 1 and 2 were co-added. Both RGS 1 and RGS 2 have a ∼3−4 Å wide gap in the spectrum as a consequence of CCD chain failure (10.4−13.8 Å for RGS 1 and 19.8−24.2 Å for RGS 2), and further small (∼0.1 Å) gaps due to the finite separation of adjacent chips.

The line parameters derived from LETGS and RGS are summarized in Tables 1 and 2. The results from the positive and negative side of the LETGS spectrum are listed separately to examine the accuracy of the wavelength calibration. We find

[3] CORA can be downloaded from `http://www.hs.uni-hamburg.de/DE/Ins/Per/Ness/Cora`

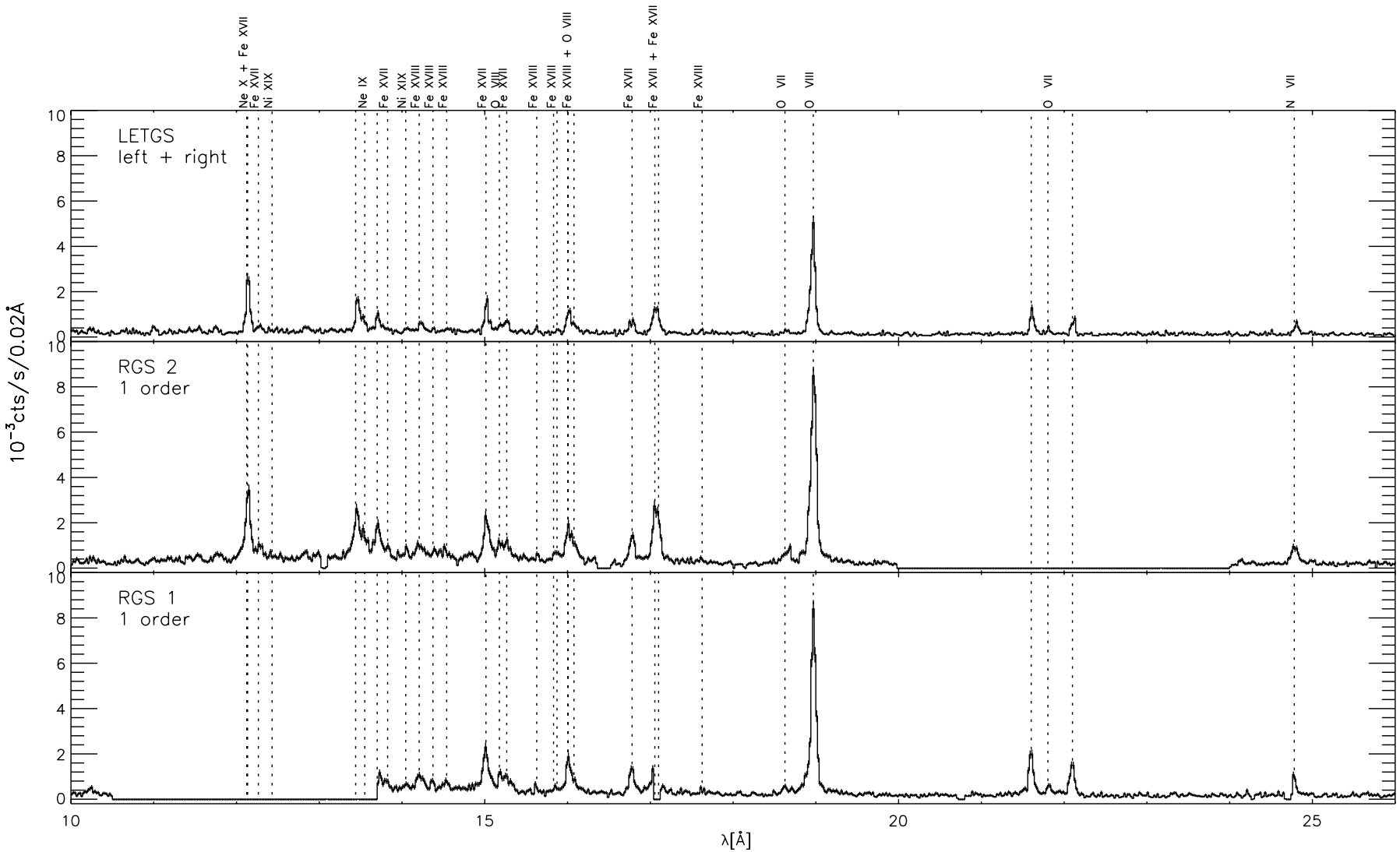

Fig. 3. Comparison of the contemporaneous *XMM-Newton* RGS 1 and RGS 2, and *Chandra* LETGS spectra of YY Gem in the range $\lambda = 10-26$ Å. Straight horizontal lines in the RGS spectra represent gaps due to CCD chain failure or individual chip separation.

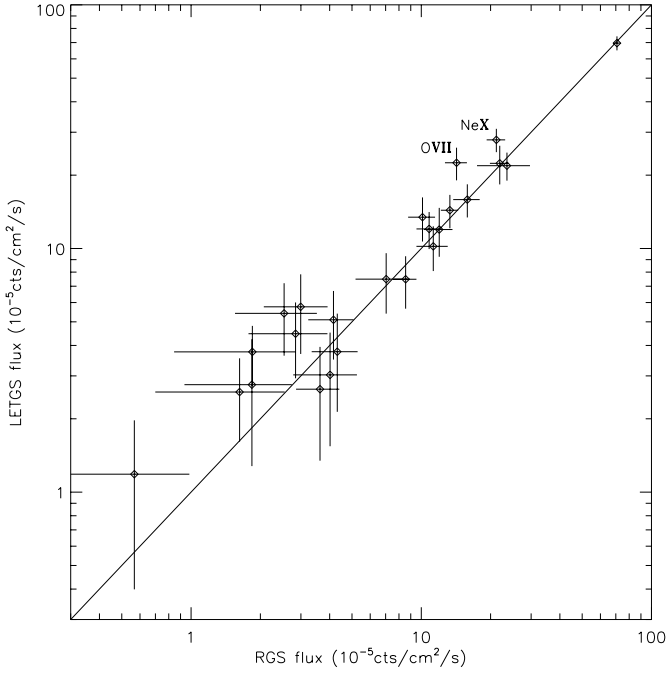

Fig. 4. Comparison of LETGS and RGS fluxes for individual emission lines; $2\,\sigma$ uncertainties.

that the line centers are in excellent agreement. Apart from the observed line center and width Tables 1 and 2 present the total number of counts I, the photon flux, and the identification and predicted line positions adopted from Mewe et al. (1985), Mewe et al. (1995), and Phillips et al. (1999). We used the effective areas of the respective instrument to compute the photon flux. The photon flux does not depend on instrumental properties and can be used for direct comparison of LETGS and RGS.

In Fig. 4 we present a comparison of the LETGS and RGS fluxes for individual lines. Our simultaneous observations allow to demonstrate that the measurements by these two instruments are consistent. Most photon fluxes are in agreement within one or two sigma. The largest deviations between LETGS and RGS occur for the O VII triplet and the Ne X Lyα line. The deviations in O VII can most likely be attributed to an oxygen absorption edge in the RGS which reduces the effective area at the position of the O VII triplet, and had not yet been corrected for in the response matrix at the time of analysis (den Herder et al. 2002). The discrepancy in Ne X seems to result from a problem in the positive side of the LETGS, as its negative side and RGS provide comparable fluxes. Note that the photon fluxes in Tables 1 and 2 denote the combined flux of both unresolved stars in the YY Gem binary.

3.2. He-like ions

The spectral ranges of the LETGS and the RGS comprise the He-like triplet transitions of several elements. In the spectrum of YY Gem the O VII triplet is by far the strongest and best resolved triplet. The Si XIII triplet is not fully resolved, and the Ne IX triplet is blended with iron lines. All other He-like ions do not produce sufficient signal. The resonance line of the N VI triplet is weakly detected in the RGS spectrum, while the intercombination and the forbidden line of N VI are not identified. In Fig. 5 we display the spectral region around the Ne IX and the O VII triplets. An iron line on the long wavelength side of the Ne IX forbidden line (at $\lambda \sim 13.83$ Å) was included in the fit. The contamination of the Ne IX triplet stems mainly from Fe XIX (at 13.53 Å) which is unresolved from the triplet intercombination line. Recall that for both the Ne IX and the O VII triplet only one RGS is available.

The only element with resolved and strong enough lines for plasma diagnostics based on an analysis of line ratios is oxygen. Note that oxygen provides only information about comparatively low temperatures ($\sim$1–4 MK). We determined the R and G ratios from the flux in the individual triplet lines. Furthermore, we computed the flux ratio between the H-like Lyα line and the He-like resonance line. This line ratio can be used as a temperature diagnostic, because the degree of ionization depends on the temperature. The result is listed in Table 3. Figure 5 shows that the strength of the r line is comparable to the sum of the intensities in the f and the i line. This is typical for a collisional plasma. It was shown by Blumenthal et al. (1972) that the UV radiation field of the star can modify the R ratio in the same way as collisional excitation, namely by depopulating the upper level of the f transition to the upper levels of the i transition. We made use of the calculations by Porquet et al. (2001), which include the radiation field of the star, to estimate the density n_e and formation temperature T of the oxygen triplet. However, as YY Gem is composed of two M-type stars it is reasonable to neglect the radiation field and assume that the relative intensities of f and i reflect the frequency of collisions and, therefore, represent a direct measure of the density. The observed G ratio corresponds to a formation temperature between 2 and 3 MK. The formation temperature defines the relation between the R ratio and the electron density (Porquet et al. 2001). The models place our measurements of R (see Table 3) in the low-density limit, where R is insensitive to density, and only an upper limit of $n_e \leq 2 \times 10^{10}$ cm^{-3} can be provided.

The plasma emissivities from the MEKAL code (Mewe et al. 1985 and Mewe et al. 1995) applied to the Lyα/r ratio result in a temperature of 3.4 ± 0.1 MK in the LETGS and 4.0 ± 0.1 MK in the RGS. These somewhat higher temperatures than those derived from the G ratio is naturally explained by the higher ionization stage of the involved species. The difference between the measurements in these two instruments probably arises from the difference in the O VII flux, which is underestimated in the RGS due to calibration problems as outlined above. We caution that given these uncertainties the absolute values for the line ratios must be treated with caution, but relative measurements comparing the same instrument (e.g. as presented in Sect. 4) are still meaningful.

3.3. Optical depth effects

The general assumption of our plasma diagnostics is that the plasma is optically thin, i.e., resonance photons are not scattered out of the line of sight as described by Schrijver et al. (1995) and Mewe et al. (1995). To check whether an optically

Table 1. Results from line fitting of the time averaged first order LETGS and RGS spectra. Positive and negative side of the LETGS are listed separately to demonstrate the accuracy of the wavelength calibration. RGS 1 and RGS 2 spectra were combined except for lines which fall in the wavelength ranges corresponding to failed CCDs or gaps between chips. Line blends are indicated by quotation marks (″). Lines which are identified but not properly resolved are marked by asterisks (*). For RGS all lines are represented by Lorentzian profiles, and for LETGS by Gaussians. The typical error on the line width is ∼0.005 Å. Line identifications are from Mewe et al. (1985), Mewe et al. (1995), and Phillips et al. (1999). Lines detected only by LETGS are listed in Table 2.

λ	σ	I	Photon Flux[a]	λ	σ	I	Photon Flux[a]	λ	σ	I	Photon Flux[a]	Identification		
[Å]	[Å]	[cts]	[10^{-5} $\frac{ph}{s\,cm^2}$]	[Å]	[Å]	[cts]	[10^{-5} $\frac{ph}{s\,cm^2}$]	[Å]	[Å]	[cts]	[10^{-5} $\frac{ph}{s\,cm^2}$]	Ion	Trans.	λ
LETGS +1 order				**LETGS -1 order**				**RGS 1 + 2**						
*6.665	0.035	36.1 ± 8.8	3.5 ± 0.8	*6.622	0.027	54.0 ± 8.8	4.8 ± 0.8	6.654	0.039	45.6 ± 12.4	1.8 ± 0.5	Si XIII	r	6.650
*″	″	″	″	*″	″	″	″	6.729	0.035	41.1 ± 11.7	1.6 ± 0.5	Si XIII	i	6.690
*6.740	0.039	18.5 ± 8.0	1.8 ± 0.8	*6.741	0.033	33.0 ± 7.8	2.9 ± 0.7	″	″	″	″	Si XIII	f	6.740
				–	–	–	–	14.050	0.044	198.4 ± 26.0	2.8 ± 0.4	Ni XIX	Ne8A	14.045
				14.208	0.036	37.8 ± 9.6	4.9 ± 1.2	14.197	0.062	352.5 ± 39.4	4.9 ± 0.5	Fe XVIII	F14	14.208
14.241	0.022	45.5 ± 9.0	6.0 ± 1.2					14.252	0.056	183.7 ± 35.6	2.5 ± 0.5	Fe XVIII	F13	14.257
–	–	–	–	–	–	–	–	14.379	0.061	212.2 ± 29.8	3.1 ± 0.4	Fe XVIII	F12	14.378
–	–	–	–	–	–	–	–	14.525	0.062	274.2 ± 30.6	3.8 ± 0.4	Fe XVIII	F10	14.540
15.036	0.022	107.9 ± 12.1	13.8 ± 1.6	15.013	0.021	118.9 ± 12.6	14.9 ± 1.6	15.017	0.048	961.0 ± 41.5	13.3 ± 0.6	Fe XVII	Ne3C	15.014
*15.183	0.023	18.4 ± 7.4	2.3 ± 0.9	*15.193	0.032	40.4 ± 9.7	5.0 ± 1.2	*15.183	0.049	282.9 ± 31.9	4.3 ± 0.5	O VIII	Lyγ	15.175
*15.262	0.025	47.4 ± 9.5	6.0 ± 1.2	*15.271	0.017	33.2 ± 8.0	4.1 ± 1.0	*15.259	0.043	270.3 ± 30.2	4.2 ± 0.5	Fe XVII	Ne3D	15.265
15.636	0.002	14.0 ± 4.7	1.8 ± 0.6	–	–	–	–	15.632	0.022	39.8 ± 14.6	0.6 ± 0.2	Fe XVIII	F7	15.628
–	–	–	–	–	–	–	–	15.861	0.037	52.4 ± 19.7	0.8 ± 0.3	Fe XVIII	F6	15.831
–	–	–	–	–	–	–	–	″	″	″	″	Fe XVIII	F5	15.874
*16.034	0.024	95.6 ± 11.5	12.3 ± 1.5	*16.004	0.025	104.0 ± 11.8	13.2 ± 1.5	*16.013	0.063	770.1 ± 45.8	10.8 ± 0.6	Fe XVIII	F4	16.002
*″	″	″	″	*″	″	″	″	″	″	″	″	O VIII	Lyβ	16.003
*16.110	0.020	36.4 ± 8.2	4.6 ± 1.0	*16.076	0.018	19.3 ± 6.8	2.4 ± 0.9	*16.080	0.066	200.0 ± 37.6	2.8 ± 0.5	Fe XVIII	F3	16.078
16.794	0.017	52.5 ± 8.7	7.3 ± 1.2	16.757	0.031	61.0 ± 10.0	7.7 ± 1.3	16.783	0.049	575.9 ± 32.9	8.6 ± 0.5	Fe XVII	Ne3F	16.780
–	–	–	–	–	–	–	–	17.612	0.019	39.5 ± 12.6	0.6 ± 0.2	Fe XVIII	F1	17.626
18.651	0.029	26.4 ± 6.9	3.8 ± 1.0	–	–	–	–	18.635	0.064	243.2 ± 25.9	3.6 ± 0.4	O VII	He3A	18.627
18.977	0.023	490.7 ± 22.8	71.4 ± 3.3	18.947	0.030	484.0 ± 22.8	67.0 ± 3.2	18.972	0.059	4630.1 ± 74.0	70.8 ± 1.1	O VIII	Lyα	18.973
–	–	–	–	–	–	–	–	28.460	0.048	72.6 ± 15.8	1.6 ± 0.3	C VI	Lyβ	28.446
–	–	–	–	–	–	–	–	28.776	0.021	35.8 ± 10.7	0.8 ± 0.2	N VI	r	28.787
33.739	0.017	55.0 ± 8.4	17.5 ± 2.7	33.745	0.026	83.4 ± 10.3	23.3 ± 2.9	33.732	0.070	662.7 ± 31.1	21.9 ± 1.0	C VI	Lyα	33.700
LETGS +1 order				**LETGS -1 order**				**RGS 1**						
21.614	0.023	82.4 ± 10.2	19.1 ± 2.4	21.613	0.022	102.8 ± 11.2	21.8 ± 2.4	21.600	0.047	475.0 ± 26.0	14.2 ± 0.8	O VII	r	21.610
21.812	0.022	19.8 ± 6.1	4.6 ± 1.4	21.810	0.018	17.6 ± 5.6	3.8 ± 1.2	21.814	0.045	99.0 ± 15.3	3.0 ± 0.5	O VII	i	21.800
22.115	0.016	53.7 ± 8.3	12.5 ± 1.9	22.108	0.022	52.7 ± 8.5	11.5 ± 1.9	22.095	0.044	332.7 ± 22.3	10.1 ± 0.7	O VII	f	22.100
LETGS +1 order				**LETGS -1 order**				**RGS 2**						
12.150	0.021	231.7 ± 16.5	32.5 ± 2.3	12.130	0.019	169.8 ± 14.4	23.1 ± 2.0	12.141	0.044	736.9 ± 34.0	21.2 ± 1.0	Ne X	Lyα	12.132
″	″	″	″	″	″	″	″	″	″	″	″	Fe XVII	Ne4C	12.134
12.291	0.019	33.5 ± 8.1	4.7 ± 1.1	12.266	0.028	10.0 ± 7.0	1.4 ± 1.0	12.282	0.050	140.1 ± 21.6	4.0 ± 0.6	Fe XVII	Ne4D	12.264
–	–	–	–	12.839	0.027	22.9 ± 8.1	3.1 ± 1.1	12.836	0.037	63.3 ± 15.5	1.8 ± 0.5	Fe XX	N16	12.834
*13.467	0.021	127.4 ± 13.1	16.7 ± 1.7	*13.465	0.025	129.3 ± 13.7	17.1 ± 1.8	*13.451	0.061	545.8 ± 35.9	15.8 ± 1.0	Ne IX	r	13.448
*13.535	0.024	40.5 ± 9.4	5.3 ± 1.2	*13.543	0.030	59.4 ± 11.1	7.8 ± 1.5	*13.539	0.072	248.5 ± 32.8	7.0 ± 0.9	Fe XIX	O15	13.524
″	″	″	″	″	″	″	″	″	″	″	″	Ne IX	i	13.553
13.720	0.024	71.9 ± 10.6	9.4 ± 1.4	13.703	0.033	79.1 ± 11.6	10.3 ± 1.5	*13.709	0.068	410.1 ± 31.8	11.3 ± 0.9	Ne IX	f	13.700
–	–	–	–	–	–	–	–	*13.831	0.057	74.3 ± 21.6	2.0 ± 0.6	Fe XVII	Ne3A	13.826
17.083	0.033	157.4 ± 14.2	23.4 ± 2.1	17.051	0.035	152.0 ± 14.1	20.8 ± 1.9	*17.050	0.053	419.9 ± 37.5	12.1 ± 1.1	Fe XVII	Ne3G	17.055
″	″	″	″	″	″	″	″	*17.095	0.052	393.9 ± 36.8	11.4 ± 1.1	Fe XVII	NeM2	17.100
24.802	0.020	34.3 ± 7.2	8.0 ± 1.7	24.810	0.027	57.5 ± 9.0	12.7 ± 2.0	24.788	0.079	331.6 ± 23.4	12.0 ± 0.8	N VII	Lyα	24.780

[a] Fluxes are not corrected for interstellar absorption.

Table 2. Emission lines observed in the time averaged positive and negative LETGS spectra outside the spectral range of or not detected by the RGS. All lines are represented by Gaussians. Line identifications are from Mewe et al. (1985), Mewe et al. (1995), and Phillips et al. (1999).

LETGS positive order				LETGS negative order						
λ	σ	I	Photon Flux	λ	σ	I	Photon Flux	Identification		
[Å]	[Å]	[ctgs]	[10^{-5} $\frac{\text{ph}}{\text{s cm}^2}$]	[Å]	[Å]	[cts]	[10^{-5} $\frac{\text{ph}}{\text{s cm}^2}$]	Ion	Trans.	λ
6.195	0.027	36.2 ± 7.6	3.5 ± 0.7	6.178	0.026	24.7 ± 6.8	2.3 ± 0.6	Si XIV	Lyα	6.180
8.437	0.019	18.7 ± 6.4	2.0 ± 0.7	8.402	0.019	20.4 ± 6.6	2.1 ± 0.7	Mg XII	Lyα	8.421
36.424	0.044	38.2 ± 7.6	13.2 ± 2.6	36.394	0.028	18.4 ± 5.5	5.6 ± 1.7	Ne X	Lyα(3.)	36.396
″	″	″	″	″	″	″	″	S XII	B6A	36.398
–	–	–	–	36.559	0.016	9.8 ± 4.0	3.0 ± 1.3	S XII	B6C	36.563
36.912	0.023	15.3 ± 4.9	5.5 ± 1.8	–	–	–	–	S X	N7	36.900
37.954	0.030	28.0 ± 6.4	11.2 ± 2.6	37.934	0.057	24.3 ± 6.9	8.6 ± 2.5	O VIII	Lyα (2.)	
44.014	0.020	30.0 ± 6.3	4.8 ± 1.0	44.024	0.032	32.5 ± 7.6	4.4 ± 1.1	Si XII	Li6A	44.020
44.176	0.025	35.1 ± 6.9	5.6 ± 1.1	44.169	0.017	30.5 ± 6.8	4.1 ± 0.9	Si XII	Li6B	44.165
56.920	0.031	41.4 ± 7.4	8.5 ± 1.5	–	–	–	–	O VIII	Lyα (3.)	
94.023	0.059	70.6 ± 9.9	28.8 ± 4.0	93.956	0.052	53.9 ± 8.7	23.3 ± 3.8	Fe XVIII	F4A	93.930
108.450	0.058	42.1 ± 8.2	22.2 ± 4.3	108.418	0.057	34.0 ± 7.6	18.6 ± 4.2	Fe XIX	O6a	108.370
117.185	0.058	46.8 ± 8.6	26.0 ± 4.8	117.184	0.085	56.6 ± 9.8	31.9 ± 5.5	Fe XXII	B11	117.170
128.818	0.049	33.4 ± 7.3	33.6 ± 7.4	128.738	0.055	27.7 ± 7.2	24.8 ± 6.5	Fe XXI	C6A	128.730
132.978	0.068	80.8 ± 10.6	81.7 ± 10.7	132.952	0.078	95.5 ± 11.4	83.6 ± 10.0	Fe XX	N6A	132.850

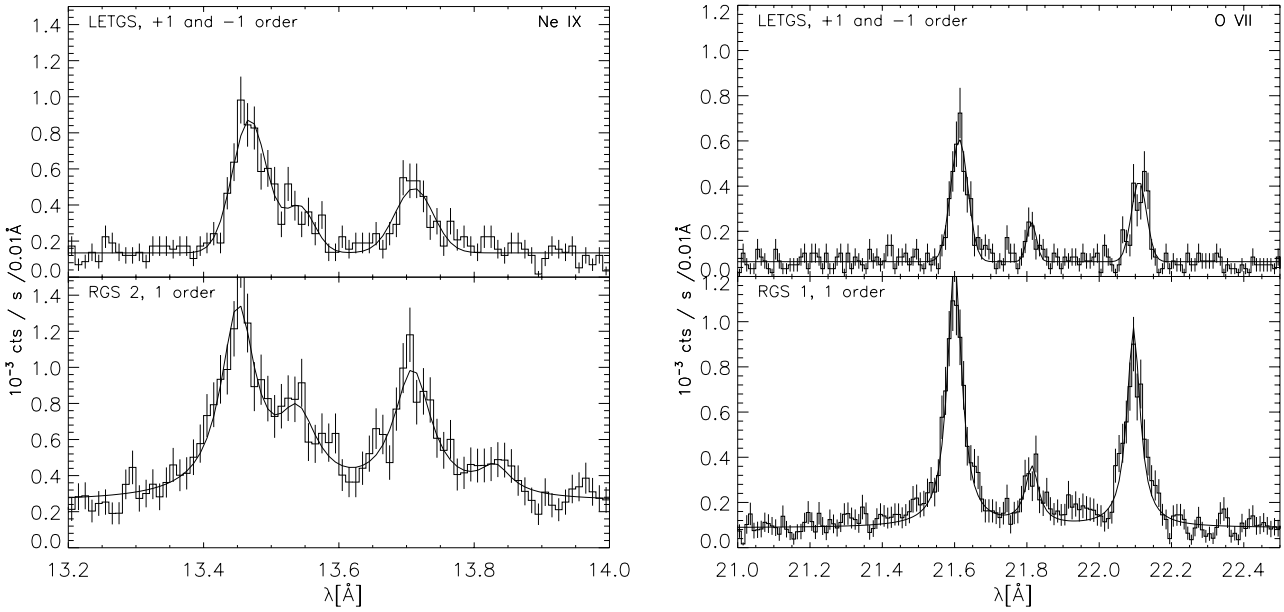

Fig. 5. He-like triplets of Ne IX and O VII measured with LETGS and RGS together with line fits. The continuum close to each triplet is approximated by a straight horizontal line. The intensity enhancement to the right of the Ne IX triplet in the RGS spectrum is due to Fe XVII. The major contamination of the Ne IX triplet comes from a Fe XIX line which is unresolved from the triplet intercombination line (see Table 1).

thin model is justified we estimate the optical depth by comparing the observed flux ratio of the resonance line of Fe XVII at 15.014 Å and the adjacent line at 15.265 Å of the same ion which has a much lower oscillator strength. The same procedure was carried out for other active stars, e.g. by Mewe et al. (2001) and Ness et al. (2002a), and they find $f_{15.014}/f_{15.265}$ = 2.85 ± 0.14 (Capella) and $f_{15.014}/f_{15.265}$ = 2.81 ± 0.25 (Algol). For Proyon we derive a ratio of 2.9 ± 1.7 using the RGS measurement given by Raassen et al. (2002). From comparison with laboratory measurements from EBIT (2.8−3.2; Brown et al. 1998) Mewe et al. (2001) and Ness et al. (2002a) concluded that the coronal plasma of Capella, Procyon and Algol is optically thin. From our observation of YY Gem we calculate a ratio of 2.8 ± 0.5 for LETGS and 3.2 ± 0.5 for RGS, compatible with the values cited above. This indicates that stellar coronae are indeed optically thin, and as the results are similar for stars with very different activity levels we conclude that optical depth effects generally are negligible in stellar coronae.

4. Time-resolved spectroscopy at high and low resolution

In this section we complement the analysis of the emission line spectrum of YY Gem with time-resolved modeling of the strongest lines seen with the RGS. The spectra discussed in the previous sections comprise the full *Chandra* and *XMM-Newton*

Table 3. Line ratios $R = f/i$, $G = (f+i)/r$, and Lyα/r for oxygen, $1\,\sigma$ uncertainties.

	LETGS		
	+1	−1	total
R	2.70 ± 0.93	3.01 ± 1.08	3.24 ± 0.82
G	0.89 ± 0.17	0.70 ± 0.13	0.77 ± 0.10
Lyα/r	3.73 ± 0.49	3.07 ± 0.36	3.35 ± 0.29
	RGS		
R			3.38 ± 0.57
G			0.92 ± 0.08
Lyα/r			4.98 ± 0.28

exposure times and represent, therefore, averages over ∼75% of the orbital period of YY Gem. The spectral shape is, however, expected to be variable (i) due to the changing aspect of the binary in the course of its orbital motion, and (ii) due to intrinsic variability related to activity on one or both of the stars.

Next to a time-resolved analysis of individual lines, we study the temporal evolution of spectral parameters by a detailed inspection of the *XMM-Newton* EPIC spectrum. Güdel et al. (2001a) analysed the EPIC spectrum from the earlier *XMM-Newton* observation using MOS 1 and MOS 2 individually for 5 different time intervals corresponding to different orbital phases of YY Gem. Here, we fit the pn and MOS 1 + 2 spectra obtained in Sep. 2000 jointly. This allows to better constrain the spectral parameters and perform a more detailed systematic analysis of time-resolved X-ray spectroscopy.

To examine the evolution of the spectrum of YY Gem we split the total observing time in several time intervals. In choosing the time bins we took into account the variability pattern in the lightcurve. We found that the LETGS data does not provide a strong enough signal for time-resolved analysis, even if left and right side of the spectrum are added. Therefore we make no further use of LETGS data for time-resolved spectroscopy. The selection of the segments for EPIC and RGS can be read out of Fig. 1.

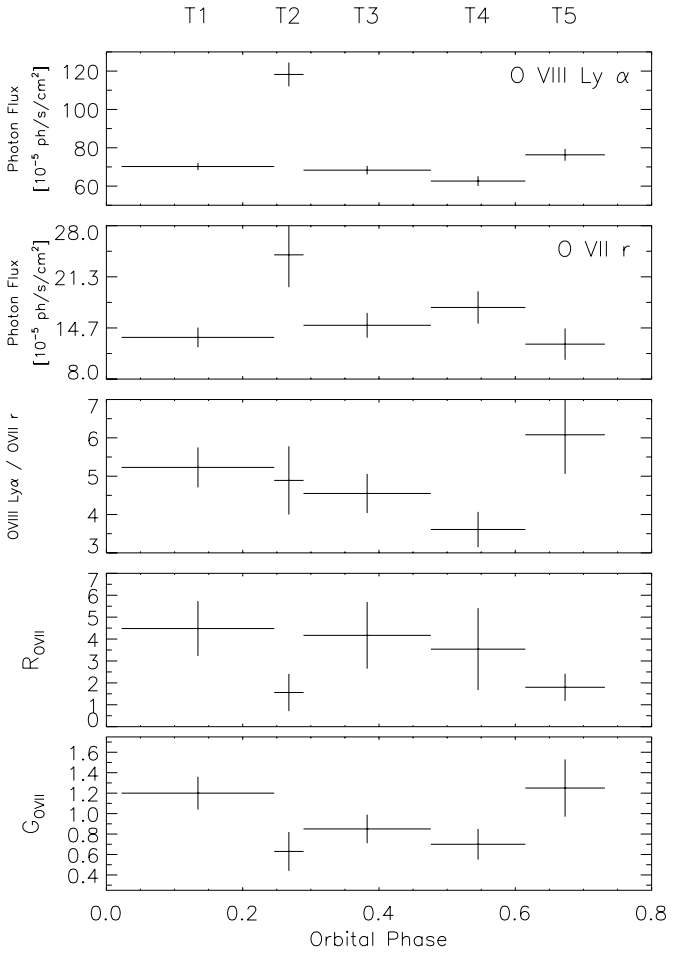

Fig. 6. Time-evolution of the O VIII H-like Lyα line and the O VII He-like resonance line, the ratio of these two lines, and the R and G ratio of the O VII triplet as observed by *XMM-Newton* RGS. Time intervals as defined in Fig. 1.

4.1. The high-resolution RGS spectrum

We extracted RGS spectra in five time intervals (see Fig. 1). Segments 2 and 5 are the phases with the highest level of activity. The strongest lines in the RGS wavelength range are examined for all five selected data segments. Some of the weaker lines are not identified at all phases. This may be due to variability of the source and/or the unequal S/N in the five intervals as a result of different exposure times. The only element which displays a strong He-like triplet and H-like Lyα in all time segments is oxygen. For this element we can refine the analysis of plasma temperature and density deriving the R and the G ratio as a function of time. It must be kept in mind, however, that oxygen probes only temperatures between 1–4 MK, and therefore does not represent the major component of the flare.

The spectra for the shorter time intervals are characterized by poor signal-to-noise. We ensured that the weak intercombination line is represented correctly by holding the separation between the line centers within the triplet fixed at the nominal value during the fitting process. In Fig. 6 we show the time evolution of O VIII and O VII and their line ratios. All ratios are characterized by rather large error bars as a result of short exposure times. A trend towards decreasing R ratio during times of enhanced activity (intervals 2 and 5) is evident although only marginally significant. To increase the significance of this result we merged the three time intervals representing the quiescent state of YY Gem, i.e., segments 1, 3, and 4, and obtained an R ratio of 3.91 ± 0.79. The difference between this time-averaged quiescent R value and the value measured during segment 2 is still only a $1.5\,\sigma$ effect, but is suggestive for a density increase as a result either of chromospheric evaporation or compression of the coronal material.

In Fig. 7 we compare the coadded RGS 1 and RGS 2 spectra during two different time intervals, segment 1 from Fig. 1 representing quiescence and segment 5 from the same figure representing a phase of strong activity. The bottom panel of the figure shows that most of the flare emission is concentrated between ∼8–16 Å. The low signal does not permit to determine whether this emission is true continuum or whether it arises from unresolved iron lines which form at high temperatures during the flare, e.g., Fe XXIV.

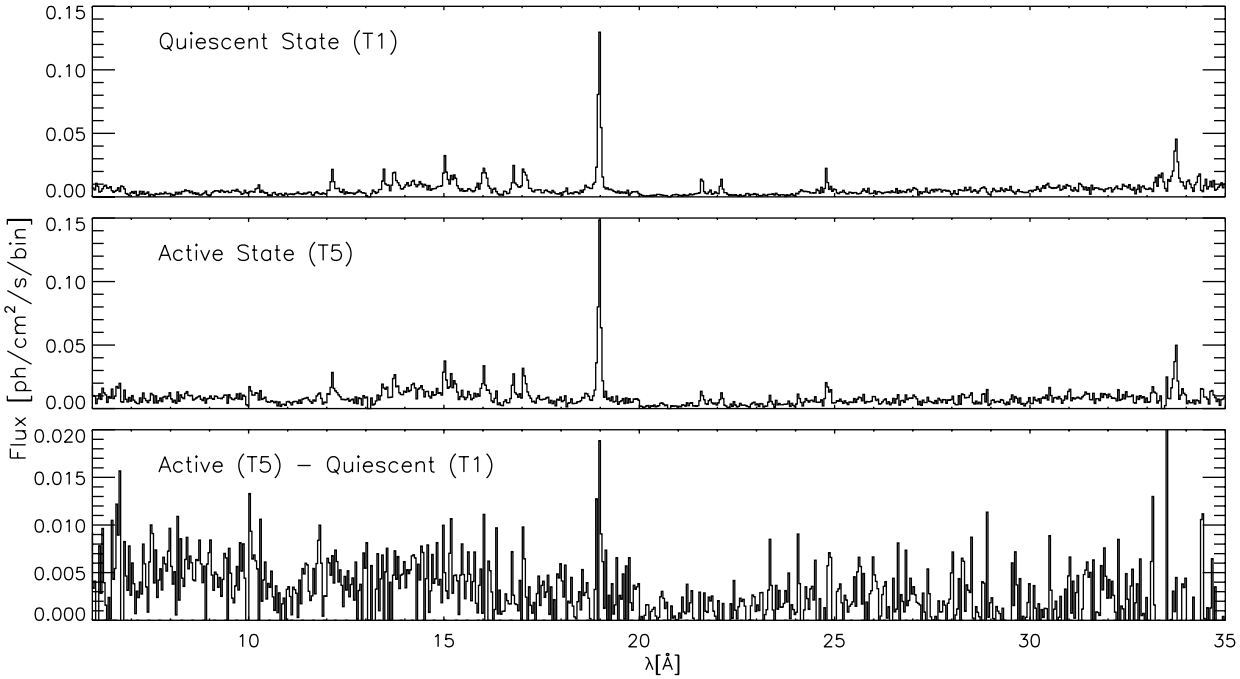

Fig. 7. Comparison of the RGS flux spectrum during quiescence (interval 1 from Fig. 1) and the most active phase (interval 5 from Fig. 1). The panel on the bottom shows the difference spectrum with significant excess emission below ∼16 Å. Binsize is 0.04 Å.

4.2. XMM-Newton *EPIC*

Due to its larger effective area the EPIC spectrum can be studied at higher time-resolution. We split the EPIC pn and MOS lightcurve in a total of 15 time intervals (see Fig. 1).

4.2.1. Photon pile-up

Photons arriving at the CCD detector can deposit energy in more than one pixel. To improve the statistics in the high-energy portion of the spectrum we include double events, i.e., photons that produced a signal in two adjacent pixels.

For bright sources (such as YY Gem) more than one photon may arrive in one pixel before the detector is read out (photon pile-up), and in addition two photons arriving at the same time in adjacent pixels are mistakenly identified as a single photon distributing its energy on both pixels. Distortions of the spectral shape due to pile-up and mis-identification of the pixel pattern distribution can safely be avoided by cutting out the central portion of the point spread function, however, at the expense of count rate statistics. In order to compromise between correction for these effects and retaining enough events to constrain spectral parameters we examined how model fits change if the photons from the innermost part of the source are excluded. For different inner radii of the source extraction area a 3-temperature VMEKAL model (see Sect. 4.2.2) gives similar plasma temperature and abundances within the statistical uncertainties. We conclude from this test that the spectral parameters are only marginally affected by pile-up in this observation, allowing us to use the full source region without having to remove the photons from the central area.

4.2.2. The quiescent spectrum

Güdel et al. (2001a) described the quiescent X-ray spectrum of YY Gem by a 3-temperature (3-T) model for thermal emission from an optically thin plasma. The existence of a multi-temperature corona on YY Gem was verified by these authors also by deriving the emission measure distribution, which showed the presence of a broad distribution of temperatures ranging from ∼2–15 MK.

We used a combination of three VMEKAL-models as implemented in XSPEC 11.0.1 to represent the spectrum in time interval t_1, when the source was in quiescence. The different instruments (pn, MOS 1, and MOS 2) were analysed jointly by multiplying the spectral model with a constant normalization factor to make up for uncertainties in the absolute calibration of the individual detectors.

We used the EPIC spectrum of phase t_1 as baseline for all other time segments in which the signal is sometimes lower due to shorter exposure time. The model parameters for the quiescent spectrum are provided in Table 4. The EPIC spectrum shows that besides the comparatively low temperatures probed by the strongest lines in the high-resolution spectrum, plasma in excess of 10^7 K is present. The observed spectrum can only be reproduced if the abundances of some elements are free fit parameters. The best fit clearly shows subsolar abundances, in particular for iron. Low abundances for elements with low First Ionization Potential (FIP) were also reported from the earlier *XMM-Newton* observation of YY Gem (see Güdel et al. 2001a).

4.2.3. Time-evolution of spectral parameters

At first we checked whether the spectrum of YY Gem can be represented by a 3-T model at all times. We assumed that the

Table 4. Spectral parameters for the quiescent state of YY Gem (derived from time interval t_1). Normalization constants to cross-calibrate the three instruments (pn, MOS 1, MOS 2) are: $N_{\rm pn} \equiv 1$ (fixed), $N_{\rm mos1} = 1.01^{+0.03}_{-0.03}$, and $N_{\rm mos2} = 1.03^{+0.03}_{-0.03}$.

kT_1	kT_2	kT_3	[keV]
$0.21^{+0.05}_{-0.07}$	$0.64^{+0.01}_{-0.02}$	$1.79^{+0.30}_{-0.24}$	
EM_1	EM_2	EM_3	[10^{51} cm^{-3}]
$2.24^{+1.87}_{-0.60}$	$13.84^{+0.82}_{-2.88}$	$2.88^{+1.05}_{-0.66}$	
O	Mg	Si	
$0.64^{+0.19}_{-0.14}$	$0.27^{+0.12}_{-0.07}$	$0.47^{+0.16}_{-0.07}$	
S	Fe	Ni	$\chi^2_{\rm red}$ (d.o.f.)
$0.50^{+0.27}_{-0.20}$	$0.23^{+0.04}_{-0.03}$	$0.00^{+0.28}_{-0.00}$	1.24 (658)

integrated light from the quiescent corona remains unaltered during the outburst. Therefore, we held all temperatures and abundances fixed and allowed only the intensity to vary, corresponding to changes in the emission measure as could be expected due to occultation effects. This way we obtained acceptable fits ($\chi^2_{\rm red} \sim 1$ and statistically distributed residuals) for all time intervals in which the star is "quiet", i.e. shows no strong variability and exhibits intensity similar to the regular non-flaring state (t_2, t_7, t_8, t_9, t_{10}, and t_{12}). During the secondary eclipse (time intervals t_8 and t_9) the emission measures EM_2 and EM_3 drop because the visible fraction of the emitting corona has decreased. After the eclipse a strong high-energy component (large EM_3) is found. These time-intervals correspond to an emission feature in the lightcurve (lasting from t_{10} to t_{12}). For t_{11}, representing the peak of this feature, we could not obtain an acceptable 3-T fit. The excess intensity in the hottest of the three components is seen already during the second half of the eclipse (t_9). This could be a hint that the emission feature fills in part of the eclipse.

At all time intervals not discussed in the previous paragraph, after fitting the 3-T model to the data a high-energy excess stands out in the residuals. This suggests that higher temperature plasma is present in addition to the emission from the quiescent corona. Adding a 4th VMEKAL component does not lead to a significant improvement. Only a 5-T model represents an adequate description of the data during the most active phases. A 5-T model was also introduced by Güdel et al. (2001a) to fit the flare observed during the first *XMM-Newton* observation of YY Gem. For the modeling we fixed spectral components #1–3 at their quiescent values (t_1; see Table 4). Generally, the statistics do not allow to constrain the abundances of the additional VMEKAL components. All abundances of components #4 and #5 were, therefore, held fixed at solar values. The "high state" (t_{15}) is an exception: Here the signal at the high-energy end of the EPIC spectrum is better than for all other time-sliced spectra. Broad emission from the Fe K complex is clearly visible at ~6.7 keV, and an acceptable solution is obtained only if the Fe abundance is a free parameter, resulting in Fe/Fe$_\odot = 0.47^{+0.10}_{-0.09}$.

We point out that we performed an additional series of spectral fits where we set the abundances of VMEKAL #4 and #5 to the quiescent values, and obtain much larger uncertainties for the model parameters. This hints at an abundance increase during active phases that seems to be not uncommon for stellar flares (Favata et al. 1999; Güdel et al. 1999).

Our modeling allows to investigate how the temperature and emission measure of the flare components behave in different stages of flares. In Fig. 8 we display both free temperatures and emission measures from the 5-T model as a function of time together with the EPIC pn lightcurve and the evolution of the luminosity as derived from the spectral fits. Both spectral components show their highest temperature during the rise phase of the lightcurve. Subsequently, the temperatures decline coherently with the intensity. The emission measure increases during the rise phase and reaches its maximum with the beginning of the decay of the lightcurve. The observed luminosity $L_{\rm x}$ ranges from (2–7.5) $\times 10^{29}$ erg/s in the EPIC band which is comparable to the values reported in the literature. The spectral parameters during extended time intervals with enhanced count rate (t_{11}, t_{15}) suggest that these are flare-like events with a strong low-T component (VMEKAL #4) and a weaker high-T component (VMEKAL #5). But note that no typical flare outburst is seen in the lightcurve for the respective time intervals.

5. Loop modeling

The size of emitting coronal structures can be estimated by help of loop models. Most of these models are based on the assumption that the plasma is confined in a single loop. While this may be adequate during simple flares, the situation in the quiescent corona is likely to be much more complex.

We used the temperature – emission measure approach which allows for heating during the flare decay, and determined the size of flaring loops from the spectral parameters of the EPIC spectra. We restricted the analysis to the first flare which is larger and longer than the second flare, and, therefore, provides better sensitivity for this kind of study.

The evolution of temperature and emission measure puts important constraints on the dynamics during flare decays. A one-dimensional hydrodynamic model describing the decay phase of solar flares was developed by Peres et al. (1987) and discussed in a series of papers (see e.g., Serio et al. 1991; Jakimiec et al. 1992; Sylwester et al. 1993; Reale et al. 1997). The model was adapted to stellar flares by Reale et al. (1997). The duration of the heating (a free parameter in the model) determines the slope ζ in the $\log T - \log \sqrt{EM}$–diagram. The limiting cases are (a) abrupt switch off, and (b) a quasi steady-state evolution for slow decay of the heating which leads to evolution along the path given by the RTV scaling law (Rosner et al. 1978). The slope ζ and the decay time of the lightcurve $\tau_{\rm LC}$ are linked by the thermodynamic decay time scale, $\tau_{\rm td}$, i.e. the decay time if heating were absent. This relation depends on instrumental properties. With the appropriate calibration ζ can be used to obtain an estimate for the half-length L of the flare loop, since according to Eq. (2) in Reale et al. (1997) L is connected to the maximum flare temperature, $T_{\rm max}$, and the thermodynamic decay time, $\tau_{\rm td}$.

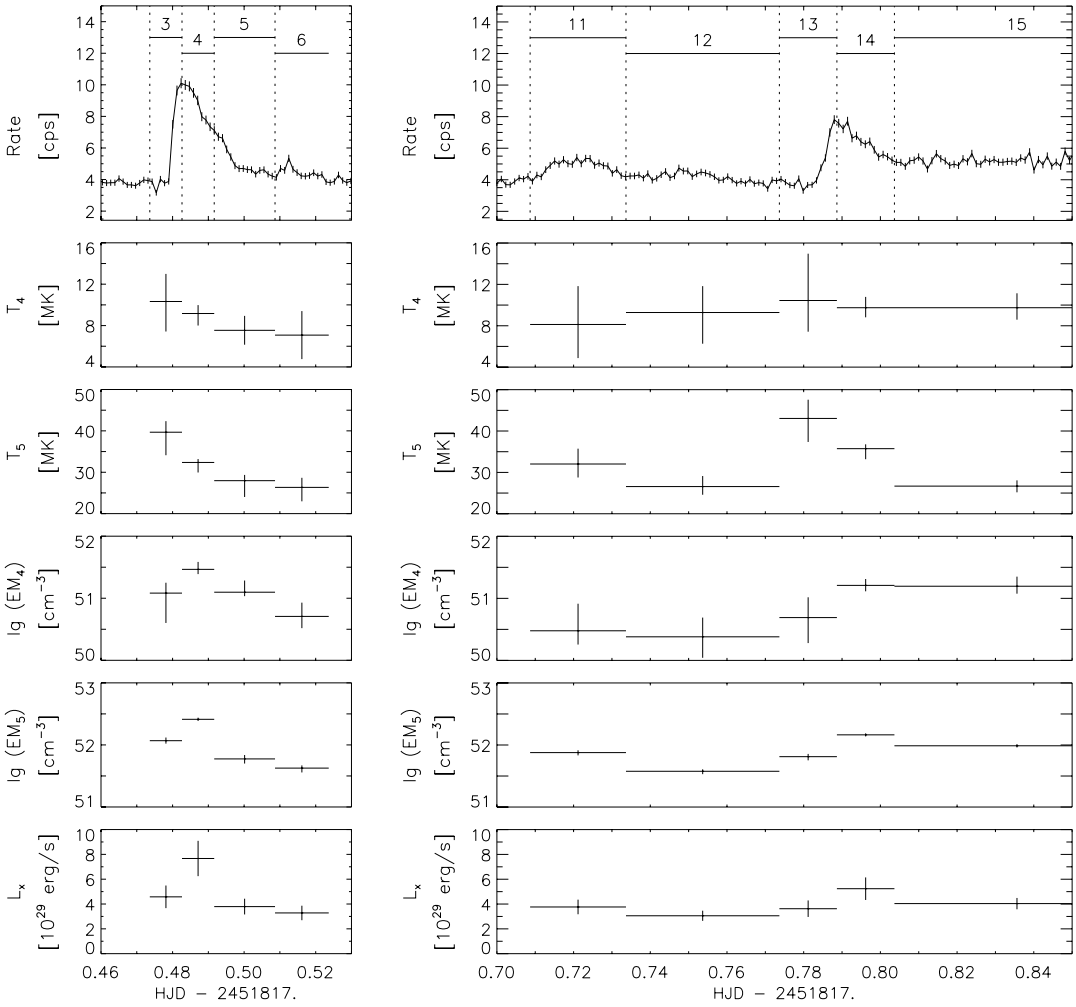

Fig. 8. Time evolution of spectral parameters during the two flares on Sep. 29/30, 2000. Shown are T_4, T_5, EM_4, and EM_5 from 5-T model fits to the joint EPIC pn + MOS spectra of YY Gem together with the pn lightcurve (top panel) and the X-ray luminosity L_x (bottom panel). The remaining three spectral components were held fixed at their quiescent values. Error bars are 90% confidence levels.

The $\log T$ − $\log \sqrt{EM}$-diagram derived from our modeling of the *XMM-Newton* EPIC spectrum during the larger flare is shown in Fig. 9. As the model was developed for a single-loop and one-temperature flare, we ignored the first component (VMEKAL #4) of the flare spectrum. This component has much smaller emission measure, i.e. the contribution to the flare emission is negligible compared to VMEKAL #5. The curve in Fig. 9 starts with the rise phase (t_3) of the flare. We measured the slope during the decay phase (t_4...t_6) and found: $\zeta = 0.21$.

We applied the model described above. Modeling the decaying part of the lightcurve by an exponential we found $\tau_{\rm LC} = 16 \pm 1$ min. The relation between ζ and $\tau_{\rm td}$ has been calibrated for EPIC-pn (Reale, priv. comm.) and yields $L = 2.0 \times 10^9$ cm for the length of the flare loop. As the low value we found for the slope ζ hints at continuous heating, the evolution of the plasma parameters can in approximation be thought of as quasi-static. Then, using the number for the loop length given above, the RTV scaling laws imply a pressure of $p \sim 6 \times 10^3$ dyne cm^{-2} for a hydrostatic loop, and a heating rate of $E_{\rm H} \sim 45$ erg cm^{-3} s^{-1}. This yields a density in the loop of $n \sim 6 \times 10^{11}$ cm^{-3}. Assuming pressure equilibrium the density at temperatures typical for the formation of O VII are estimated to be ∼10 times as high. This contrasts with the low-density limit found from the analysis of the time-averaged O VII triplet, but is consistent with the high R ratio found during the flare. Therefore, the loop model underlines the indications for increased density during flares described in Sect. 3.

6. Summary and conclusions

In September 2000 YY Gem was observed simultaneously by *XMM-Newton* and *Chandra* providing a possibility to cross-check the performance of the instruments on both satellites. We found that the line centers and the line fluxes measured by LETGS and RGS are in good agreement with only few exceptions. One of these is the underestimation of the O VII resonance line flux due to an absorption edge in the RGS which was not yet taken account of in the response matrix at the time of analysis (den Herder et al. 2002): for the resonance line of the O VII triplet the RGS flux is found to be ∼70% of the LETGS flux, but the measurements of the two instruments are

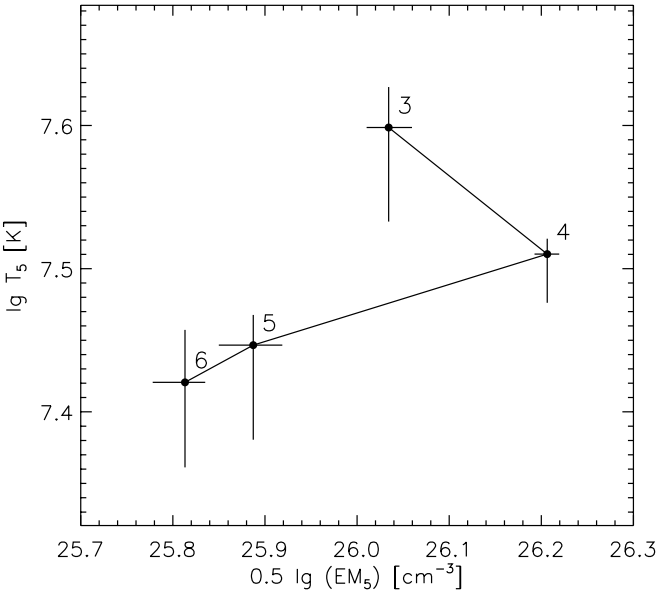

Fig. 9. Temperature – emission measure – diagram for VMEKAL component #5 for the larger of the two flares in the Sep. 2000 *XMM-Newton* EPIC observation of YY Gem. The numbers next to the data points indicate the respective time intervals.

compatible with each other at the 3 σ level. We note that similar differences have been observed between LETGS and RGS for Procyon (see Raassen et al. 2002). A deviation of the flux for the Ne X Lyα line between the two sides of the LETGS seems to point at a problem on the right side of this detector at the respective wavelength (12.13 Å).

The high-resolution spectrum of YY Gem is dominated by oxygen and neon lines and lines from intermediate ionization stages of iron, generally Fe XVIII and below. Only few lines from highly ionized iron (Fe XIX and higher) are seen at the long wavelength end of the LETGS spectrum. The characteristic Fe XXI line at 128.73 Å is detected but very weak, underlining that the corona of YY Gem is not dominated by the high temperatures (≥4 MK) typically observed on RS CVn binaries (see e.g., Mewe et al. 2001; Audard et al. 2001).

We have probed the optical depth in the corona of YY Gem using characteristic ratios of Fe XVII line fluxes. Comparing these ratios with measurements for other stars known to exhibit very different activity levels shows that optical depth effects do not play a role in stellar coronae of all types.

The correlation between X-ray luminosity and temperature in stellar coronae is well known (see e.g., Güdel et al. 1997). Now, the dispersive instruments of *Chandra* and *XMM-Newton* allow to confirm this relation using intensity ratios of individual emission lines. Ness et al. (2002b) show in their comparison of *Chandra* observations of ten stars that YY Gem fits well into the relation between L_x and temperature probed by the O VIII to O VII flux ratio representing a moderately active star.

The only element in the spectrum of YY Gem with a sufficiently strong and unblended helium-like triplet is oxygen. The $R = f/i$ value derived from the observation presented here is compatible with an earlier measurement by Güdel et al. (2001a). For the time-averaged spectrum the ratios of the oxygen triplet yield a temperature of $T = 2$–3 MK and an upper limit to the electron density of $n_e \leq 2 \times 10^{10}$ cm^{-3}. During the time of observation YY Gem showed strong variability including two flares. The time-resolved analysis of the high-resolution spectrum reveals variations of R which are suggestive of an increase in density during times of enhanced count rate. Our measurement is one of the first direct indications for the increase of the coronal density during flares on stars other than the Sun derived from high-resolution X-ray spectroscopy. A density measurement in the corona of AB Dor using an *XMM-Newton* measurement of oxygen triplet lines, e.g., resulted in comparable densities during flare and during quiescence (Güdel et al. 2001b). A detailed investigation of line ratios in the short time intervals representative for the different activity levels of YY Gem is constricted by low S/N. The time-resolved high-resolution spectroscopy, furthermore, shows that during flares the absolute amount of (oxygen emission by) relatively low-temperature plasma increases. Lines from elements probing higher temperatures more typical for flares were not strong enough for this kind of analysis.

The presence of higher temperatures in the corona of YY Gem is, however, evident from our time-resolved spectroscopy with EPIC. The temperatures for the global fit of the quiescent EPIC spectrum (2.4 MK, 7.4 MK, and 20.8 MK) comprise the temperature range measured from the analysis of oxygen lines, but go well beyond these values. Two additional VMEKAL components are necessary to describe the EPIC spectrum during flares. The corresponding temperatures and emission measures are highest during the rise phase. An attempt to reproduce the EPIC spectrum with a number of Gaussian profiles using the information from the RGS spectrum was described by Haberl et al. (2002). But the low resolution of EPIC makes this instrument insensitive to changes in the relative strength of nearby emission lines during different phases of activity.

With plasma parameters derived from spectral modeling the size of the (flare) emitting structures can be inferred. We used a hydrodynamic approach (see Reale et al. 1997) involving heating during the decay phase to determine the length of flaring loops on YY Gem. The overall size of quiescent stellar coronae can be estimated making use of plasma density and temperature derived from the analysis of high-resolution spectra (see e.g., Ness et al. 2001; Mewe et al. 2001, and Raassen et al. 2002). However, loop lengths derived from individual lines refer only to a very limited temperature range and the relevance of the single loop model for the quiescent corona is questionable. In our case the spectral parameters derived from individual lines are not useful for this kind of analysis, since the upper limits on the density translate to lower limits of the loop size according to the RTV-laws. Instead, we derived loop sizes using results from global fitting with EPIC. We find that loops are small (2×10^9 cm), on the order of a few percent of the stellar radius ($R_* \sim 0.6\ R_\odot$) of each of the components in the YY Gem binary. This is consistent with the compactness of the corona established from eclipse mapping for the earlier *XMM-Newton* observation of YY Gem (Güdel et al. 2001a). Small loops point at magnetic activity on the individual stars rather than large scale structures associated with overlapping

magnetospheres. Furthermore, the RTV-laws point at high densities in the loop, confirming the evidences for low R ratio during times of flares.

Acknowledgements. BS wishes to thank D. Grupe and F. Haberl for helpful discussions on the RGS and EPIC data analysis. We would like to thank the referee R. Pallavicini for helpful comments. BS, VB, and RN are supported by the BMBF/DLR under grant numbers 50 OR 0104, 50 OX 0001, and 50 OR 0003, respectively. The PSI group acknowledges support from the Swiss National Science Foundation (grant 2100-049343). JUN acknowledges financial support from DLR under 50 OR 98010, and NG acknowledges financial support from the European Union (HPMF-CT-1999-00228). This work is based on observations obtained with *XMM-Newton*, an ESA science mission with instruments and contributions directly funded by ESA Member States and the USA (NASA).

References

Aschenbach, B. 2002, in X-ray Optics for Astronomy: Telescopes, Multilayers, Spectrometers, and Missions, ed. P. Gorenstein, & R. B. Hoover, Proc. SPIE, 4496, 8
Audard, M., Güdel, M., & Mewe, R. 2001, A&A, 365, L329
Blumenthal, G. R., Drake, G. W. F., & Tucker, W. H. 1972, ApJ, 172, 205
Bopp, B. W., & Evans, D. S. 1973, MNRAS, 164, 343
Brinkman, A. C., Gunsing, C. J. T., Kaastra, J. S., et al. 2000, ApJ, 530, L111
Brown, G. V., Beiersdorfer, P., Liedahl, D. A., et al. 1998, ApJ, 502, 1015
Burwitz, V., Zavlin, V. E., Neuhäuser, R., et al. 2001, A&A, 379, L35
Caillault, J.-P. 1982, AJ, 87, 558
den Herder, J. W., et al. 2002, in New Visions of the X-ray Universe in the *XMM-Newton* and *Chandra* Era, 26–30 Nov. 2001, ESTEC, The Netherlands, ESA SP-488, in press
den Herder, J. W., Brinkman, A. C., Kahn, S. M., et al. 2001, A&A, 365, 7
Doyle, J. G., & Mathioudakis, M. 1990, A&A, 227, 130
Doyle, J. G., van den Oord, G. H. J., Butler, C. J., & Kiang, T. 1990, A&A, 232, 83
Favata, F., & Schmitt, J. H. M. M. 1999, A&A, 350, 900
Golub, L., Harnden, F. R., & Maxson, C. W. 1983, ApJ, 271, 264
Gotthelf, E. V., Jalota, L., Mukai, K., & White, N. E. 1994, ApJ, 436, L91
Güdel, M., Guinan, E. F., & Skinner, S. L. 1997, ApJ, 483, 947
Güdel, M., Linsky, J. L., Brown, A., & Nagase, F. 1999, ApJ, 511, 405
Güdel, M., Audard, M., Magee, H., et al. 2001a, A&A, 365, L344
Güdel, M., Audard, M., Briggs, K., et al. 2001b, A&A, 365, L336
Gunn, A. G., Migenes, V., Doyle, J. G., et al. 1997, MNRAS, 287, 199
Gunn, A. G., Brady, P. A., Migenes, V., et al. 1999, MNRAS, 304, 611
Haisch, B. M., Schmitt, J. H. M. M., Rodonó, M., & Gibson, D. M. 1990, A&A, 230, 419
Haberl, F., Bennie, P. J., Briel, U. G., et al. 2002, in New Visions of the X-ray Universe in the *XMM-Newton* and *Chandra* Era, 26–30 Nov. 2001, ESTEC, The Netherlands, ESA SP-488, in press
Hatzes, A. P. 1995, in Stellar Surface Structure, IAU Symp., 176, 90
Jakimiec, J., Sylwester, B., Sylwester, J., et al. 1992, A&A, 253, 269
Jansen, F., Lumb, D., Altieri, B., et al. 2001, A&A, 365, 1
Kron, G. E. 1952, ApJ, 115, 301
Mewe, R., Gronenschild, E. H. B. M., & van den Oord, G. H. J. 1985, A&AS, 62, 197
Mewe, R., Kaastra, J. S., Schrijver, C. J., van den Oord, G. H. J., & Alkemade, F. J. M. 1995, A&A, 296, 477
Mewe, R., Raassen, A. J. J., Drake, J. J., et al. 2001, A&A, 368, 888
Ness, J.-U., Mewe, R., Schmitt, J. H. M. M., et al. 2001, A&A, 367, 282
Ness, J.-U., Schmitt, J. H. M. M., Burwitz, V., et al. 2002a, A&A, 387, 1032
Ness, J.-U., Schmitt, J. H. M. M., Mewe, R., et al. 2002b, A&A, submitted
Pallavicini, R., Tagliaferri, G., Pollock, A. M. T., Schmitt, J. H. M. M., & Rosso, C. 1990, A&A, 227, 483
Peres, G., Reale, F., Serio, S., & Pallavicini, R. 1987, ApJ, 312, 895
Pettersen, B. R. 1976, Inst. Theor. Astrophys., Blindern-Oslo, Rep. 46, 1
Phillips, K. J. H., Mewe, R., Harra-Murnion, L. K., et al. 1999, A&AS, 138, 381
Porquet, D., & Dubau, J. 2000, A&AS, 143, 495
Porquet, D., Mewe, R., Dubau, J., Raassen, A. J. J., & Kaastra, J. S. 2001, A&A, 376, 1113
Raassen, A. J. J., Mewe, R., Audard, M., et al. 2002, A&A, 389, 228
Reale, F., Betta, R., Peres, G., Serio, S., & McTiernan, J. 1997, A&A, 325, 782
Rosner, R., Tucker, W. H., & Vaiana, G. S. 1978, ApJ, 220, 643
Schmitt, J. H. M. M., Güdel, M., & Predehl, P. 1994, A&A, 287, 843
Schmitt, J. H. M. M., & Favata, F. 1999, Nature, 401, 44
Schrijver, C. J., Mewe, R., van den Oord, G. H. J., & Kaastra, J. S. 1995, A&A, 302, 438
Serio, S., Reale, F., Jakimiec, J., Sylwester, B., & Sylwester, J. 1991, A&A, 241, 197
Strüder, L., Briel, U., Dennerl, K., et al. 2001, A&A, 365, 18
Sylwester, B., Sylwester, J., Serio, S., et al. 1993, A&A, 267, 586
Torres, G., & Ribas, I. 2002, ApJ, 567, 1140
Turner, M. J. L., Abbey, A., Arnaud, M., et al. 2001, A&A, 365, 27
Uchida, Y., & Sakurai, T. 1983, in Activity in Red-Dwarf Stars, ed. P. B. Byrne, & M. Rodonó (Reidel), 629
Vaiana, G. S., Cassinelli, J. P., Fabbiano, G., et al. 1981, ApJ, 244, 163